Chemical Engineering Journal 437 (2022) 135413

Contents lists available at ScienceDirect

Chemical Engineering Journal

journal homepage: www.elsevier.com/locate/cej

Li^+ conduction in aliovalent-substituted monoclinic Li_2ZrCl_6 for all-solid-state batteries: $Li_{2+x}Zr_{1-x}M_xCl_6$ (M = In, Sc)

Hiram Kwak [a], Daseul Han [b], Jun Pyo Son [a], Jong Seok Kim [a], Juhyoun Park [a], Kyung-Wan Nam [b], Hyungsub Kim [c,*], Yoon Seok Jung [a,*]

[a] Department of Chemical and Biomolecular Engineering, Yonsei University, Seoul 03722, South Korea
[b] Department of Energy and Materials Engineering, Dongguk University, Seoul 04620, South Korea
[c] Korea Atomic Energy Research Institute, Daejeon 34057, South Korea

ARTICLE INFO

Keywords:
All-solid-state batteries
Solid electrolytes
Halides
Ionic conductivities
Li-ion batteries

ABSTRACT

Newly emerging halide superionic conductors with excellent (electro)chemical oxidation stability and deformability are considered as the enabler for high-performance all-solid-state batteries. Compared to close-packed monoclinic Li_3InCl_6 or Li_3ScCl_6, despite the same structural framework, the lower ionic conductivity of Li_2ZrCl_6 is intriguing. Herein, the structural evolution and Li^+ migration of aliovalent-substituted Li_2ZrCl_6 with In^{3+} (or Sc^{3+}) are investigated. A monoclinic crystal structure over the entire range of substitution ($0 \leq x \leq 1.0$ in $Li_{2+x}Zr_{1-x}In_xCl_6$) is identified by the Rietveld refinement of neutron diffraction. By the aliovalent substitution, the Li^+ conductivity of Li_2ZrCl_6 is increased drastically from 7.1×10^{-6} to max. 2.1×10^{-3} S cm^{-1} at 30 °C. It is revealed that the aliovalent substitution results in anisotropic lattice volume expansion and redistribution of Li in the lattice. Specifically, the increased concentration of Li^+ in the (002) plane renders the Li^+ migration more favorable. The bond valence energy level calculations also disclose two dimensionally (2D) preferable 3D Li^+ migration channels, which emphasizes a tetrahedral Li site in the (002) plane as the key for facile Li^+ migration. Furthermore, the excellent electrochemical performance of all-solid-state batteries using In-substituted Li_2ZrCl_6 is demonstrated for single-crystalline $LiNi_{0.88}Co_{0.11}Mn_{0.01}O_2$ cathode.

1. Introduction

As climate change and increase in pollution demand electrical transportation, innovation of Li-ion batteries with respect to energy density and safety becomes inevitable [1], which can be achieved by developing all-solid-state batteries (ASSBs) with inorganic superionic conductors [2–11]. Until now, several classes of inorganic solid electrolytes (SEs) with acceptable ionic conductivities of $\geq 10^{-3}$ S cm^{-1} have been developed: sulfides (e.g., $Li_{6-y}PS_{5-y}X_{1+y}$ (X = Cl, Br; y = 0.0–0.5), 1–10 mS cm^{-1}) [12], oxides (e.g., $Li_7La_3Zr_2O_{12}$, 0.1–1 mS cm^{-1}) [13], borohydrides (e.g., $0.7Li(CB_9H_{10})$-$0.3Li(CB_{11}H_{12})$, 6.7 mS cm^{-1}) [14,15], and halides (e.g., Li_3YX_6 (X = Cl, Br), 0.51–1.7 mS cm^{-1}) [6,16]. The oxide and sulfide SEs exhibit distinct advantages and disadvantages. The excellent electrochemical stability and nominal chemical stability of oxide SEs are offset by brittleness, which makes them difficult to integrate into all-solid-state batteries without the aid of liquid or polymer electrolytes [13,17–19]. In contrast, cold pressing of "deformable" sulfide SEs has been widely applied to fabricate ASSBs [3,7,10]. However, the electrochemical stability windows of sulfide SEs are narrow. Specifically, sulfide SEs are not compatible with conventional 4 V class layered $LiMO_2$ (M = Ni, Co, Mn, Al) cathodes without protective coatings [20,21]. Further, exposure of sulfide SEs to humid air results in the emission of toxic H_2S gas [7,22–25].

In 2018, Hasegawa and coworkers reported promising results on halide SEs: trigonal Li_3YCl_6 and monoclinic Li_3YBr_6 exhibit high Li^+ conductivities of 0.51 and 1.7 mS cm^{-1}, respectively, which has led to extensive search on new halide SEs [16,26–32]. The ionic radii of monovalent halide anions are similar to or larger than those of divalent sulfide anions. This feature indicates weak metal-halide bonds and high polarizabilities, which would result in high deformability [33]. This is in agreement with the experimental observations. The weak bond strength between the monovalent halide anion and Li^+, accounts for the high Li^+ conductivity [33]. In particular, chloride compounds show excellent (electro)chemical oxidation stability, resulting in high electrochemical performance of all-solid-state batteries when combined with $LiMO_2$ cathodes [16,27,33].

* Corresponding authors.
E-mail addresses: hyungsubkim@kaeri.re.kr (H. Kim), yoonsjung@yonsei.ac.kr (Y.S. Jung).

https://doi.org/10.1016/j.cej.2022.135413
Received 19 December 2021; Received in revised form 3 February 2022; Accepted 20 February 2022
Available online 23 February 2022

The ionic radius of the central metal element in halide SEs is the main factor governing the structural framework [34,35]. Based on the results of single-crystal X-ray diffraction (XRD) analysis, Meyer and coworkers identified three different crystal structures of Li_3ErCl_6 (trigonal, $P\bar{3}m1$), Li_3YbCl_6 (orthorhombic, *Pnma*), and Li_3ScCl_6 (monoclinic, *C2/m*) [34]. Substitution of the central metal cation affects the crystal structure of the halide SEs by changing the average radius of central cation. Nazar and coworkers reported the structural evolution of Zr-substituted Li_3MCl_6 (M = Y, Er) with increased ionic conductivities, from trigonal to orthorhombic I and II structures [27], which can be explained by the smaller ionic radius of Zr^{4+} (86 pm) than that of Y^{3+} (104 pm) or Er^{3+} (103 pm). This behavior was similar to that observed in Zr^{4+} or Hf^{4+} (Hf^{4+} = 85 pm)-substituted Li_3YbCl_6 (Yb^{3+} = 100.8 pm), which was heat-treated to 500 or 650 °C [34,36].

The crystal structure of halide SEs is also affected by the synthesis method. Highly crystalline Li_3YCl_6, prepared by conventional solid-state synthesis at elevated temperatures exhibited relatively low Li^+ conductivity of ~ 0.01 mS cm^{-1}. In contrast, mechano-chemically synthesized SEs exhibited higher Li^+ conductivity of ~ 0.5 mS cm^{-1} [16]. Based on the pair distribution function and XRD analyses, Zeier and coworkers suggested that the mechano-chemically-synthesized Li_3YCl_6 with M2/M3 metal site disordering provides facile Li^+ conduction channels [37]. Sun et al. and Nazar et al. reported independently on Sc-based halide SEs with the same chemical composition, but different crystal structures with respect to various heat treatment conditions: monoclinic Li_3ScCl_6 (max. 3 mS cm^{-1}) synthesized by heating to 650 °C for 12 h [38] and disordered spinel $Li_2Sc_{2/3}Cl_4$ (1.5 mS cm^{-1}) synthesized by heating to 650 °C for 48 h [28]. Recently, our group reported on the variation in the structure of $Li_{3-x}Yb_{1-x}M_xCl_6$ (M = Zr, Hf) with respect to various heat treatments [36]. $Li_{3-x}Yb_{1-x}M_xCl_6$ crystallized from trigonal to monoclinic by substitution and from orthorhombic I to orthorhombic II when prepared at 400 and 500 °C, respectively.

Li_2ZrCl_6 is an intriguing compound in terms of ionic radius and synthesis method [29]. Since the ionic radius of Zr^{4+} (86 pm) is similar to that of Mg^{2+} (86 pm) or Sc^{3+} (88.5 pm), Li_2ZrCl_6 is expected to form a disordered spinel or monoclinic structure. However, mechano-chemically prepared Li_2ZrCl_6 belonged to the hexagonal close-packed (hcp) trigonal Li_3YCl_6 (space group $P\bar{3}m1$) group, and it showed a Li^+ conductivity of 4.0×10^{-4} S cm^{-1} at 30 °C [16,37]. In contrast, Li_2ZrCl_6 prepared at 260 °C exhibited a monoclinic structure, which is isostructural with Li_3InCl_6 and Li_3ScCl_6, but with a considerably low Li^+ conductivity of 5.7×10^{-6} S cm^{-1} [26,29,38]. Recently, Zeier and coworkers investigated the effects of the aliovalent substitution of Li_3InCl_6 with Zr [39]. However, the range of the exploration was limited from x = 0.0 to 0.5 in $Li_{3-x}In_{1-x}Zr_xCl_6$, and the origin of the low Li^+ conductivity of monoclinic Li_2ZrCl_6 has remained elusive.

Inspired by these previous studies, we investigated the structural evolution and Li^+ conduction in M^{3+}-substituted Li_2ZrCl_6 ($Li_{2+x}Zr_{1-x}M_xCl_6$, M = In, Sc), synthesized by heat treatment, over the entire range of x ($0 \le x \le 1$). $Li_{2+x}Zr_{1-x}M_xCl_6$ exhibited a monoclinic crystal structure with *C2/m* symmetry in this solid solution series. In^{3+}-substituted Li_2ZrCl_6 showed a maximum conductivity of 2.1 mS cm^{-1} at 30 °C with the lowest activation energy of 0.309 eV ($Li_{2.7}Zr_{0.3}In_{0.7}Cl_6$). Rietveld refinement of neutron diffraction (ND), high-resolution powder X-ray diffraction (HRPD), and bond valence energy landscape (BVEL) calculations revealed the three-dimensional (3D) Li^+ conduction pathways, for which the Li^+ concentration in the (0 0 2) plane was significant. The excellent compatibility of In^{3+}-substituted Li_2ZrCl_6 with single-crystalline $LiNi_{0.88}Co_{0.11}Mn_{0.01}O_2$ (single-NCM88) in all-solid-state cells was also demonstrated.

2. Results and discussion

$Li_{2+x}Zr_{1-x}In_xCl_6$ powders were prepared by ball-milling a stoichiometric mixture of LiCl, $InCl_3$, and $ZrCl_4$, followed by heating to 260 °C for 12 h. Field-emission scanning electron microscopy (FESEM) images of Li_2ZrCl_6 and $Li_{2.5}Zr_{0.5}In_{0.5}Cl_6$ powders showed their similar particle sizes and morphologies (Figure S1). The powder ND patterns of $Li_{2+x}Zr_{1-x}In_xCl_6$ over the entire range of x ($0 \le x \le 1.0$) are shown in Fig. 1a, and the HRPD patterns using synchrotron radiation are shown in Figure S2. All the patterns correspond to the monoclinic Li_2ZrCl_6 with a space group *C2/m*, implying the formation of a solid-solution phase over the entire range of x ($0 \le x \le 1.0$). Crystal structures of the $Li_{2+x}Zr_{1-x}In_xCl_6$, shown in Fig. 1b, visualize four types of octahedra and a single type of tetrahedra. The specific structures are isolated $[Zr/In]Cl_6$ octahedra, $LiCl_6$ octahedra (where metal partially occupies in the (0 0 1) plane), two kinds of $LiCl_6$ octahedra, and $LiCl_4$ tetrahedra in the (0 0 2) plane, and each of these structures correspond to the metal sites of M1, M2/Li3, Li1, Li2, and Li4 sites, respectively. Interestingly, the metal layers (each $[Zr/In]Cl_6$ octahedron is surrounded by six $LiCl_6$ octahedra) and Li layer (containing only $LiCl_6$ octahedra) show a honeycomb type of ordering, which is common in an O3 stacking model of Li_2MnO_3 cathode materials [40,41]. A few weak reflections observed in $Li_{2+x}Zr_{1-x}In_xCl_6$ over the entire range of x in the 2θ range of 15–26°, were also reported in previous reports on Li_2MnO_3, which is expected to originate from stacking faults. This tendency was confirmed from the HRPD patterns (indicated by red arrows in Figure S2) [40,41]. Extensive structural studies, such as high-resolution transmission electron microscopy, could further reveal the stacking faults of $Li_{2+x}Zr_{1-x}In_xCl_6$ [41,42].

In the HRPD patterns (Figure S2), which offer better sensitivity and resolution at low angles, compared to the ND patterns, the increase in In^{3+} resulted in peak shifts at low angles. The peak corresponding to the (0 0 1) planes at ~ 14.8° was dramatically shifted in the negative direction, which is in contrast to the marginal shifts of the peak corresponding to the (0 2 0) planes at 15.8° (Figure S2). This observation reflects the asymmetric expansion of the lattice volume along the *c* direction. The corresponding changes in lattice constant, unit cell angle (β), and lattice volume as a function of In^{3+} substitution are shown in Fig. 1c, d, and e, respectively. Upon In^{3+}-substitution, the change in the c-axis was the largest (+1.24%), whereas the changes in the a and c-axes were 0.24% and 0.34%, respectively. This result indicates why the shift for the (0 0 1) peak in the HRPD pattern (Figure S2) was larger than those for other peaks. Furthermore, other peaks due to the stacking fault were broad, which makes the peak shifts difficult to detect. Upon increasing x in $Li_{2+x}Zr_{1-x}In_xCl_6$, the lattice parameters, *a* and *c*, increased with approximate linearity. This behavior is expected, considering the larger ionic radius of In^{3+} (94 pm), compared to that of Zr^{4+} (86 pm). However, the change in *b* was nonlinear, and the maximum value for *b* was obtained at x = 0.8. This non-uniform increase in each lattice parameter indicates the asymmetric expansion of the lattice volume, which was also confirmed by the unit cell angle (Fig. 1d) and lattice volume results (Fig. 1e). Interestingly, when Sc^{3+} (88.5 pm), which is smaller than In^{3+} (94 pm) and similar in size to Zr^{4+} (86 pm), was substituted, anisotropic expansion of the lattice parameter was also observed (Figure S3). These results suggest that apart from ionic radius, there are many factors that affect the asymmetric volume expansion in the aliovalent-substituted Li_2ZrCl_6.

The nonlinear changes in the lattice parameters, *b* and β, seem to be related to the mixed ionic–covalent bonding character, such as between Zr–Cl and In (or Sc)–Cl bonds. In previous X-ray absorption near-edge structure studies, the covalent ligand orbital mixing in Sc–Cl and In–Cl bonds was proved by the pre-edge features of Cl K-edge spectra. [26,38,43] However, the Zr–Cl bonds showed the absence of the pre-edge peak in Cl K-edge spectra; therefore, they are considered to exhibit mainly ionic bond character [29]. The oxide materials with ionic bonding characteristics upon substitution with a metal exhibiting a tendency to form covalent bonds, distortion of the crystal structure occurs [44,45], which is explained by the anisotropic change in bond length of the original polyhedra. From our previous results, $ZrCl_6$ octahedra with mainly ionic bonding character were also distorted when substituted with Fe^{3+}, which exhibit covalent bonding characteristic

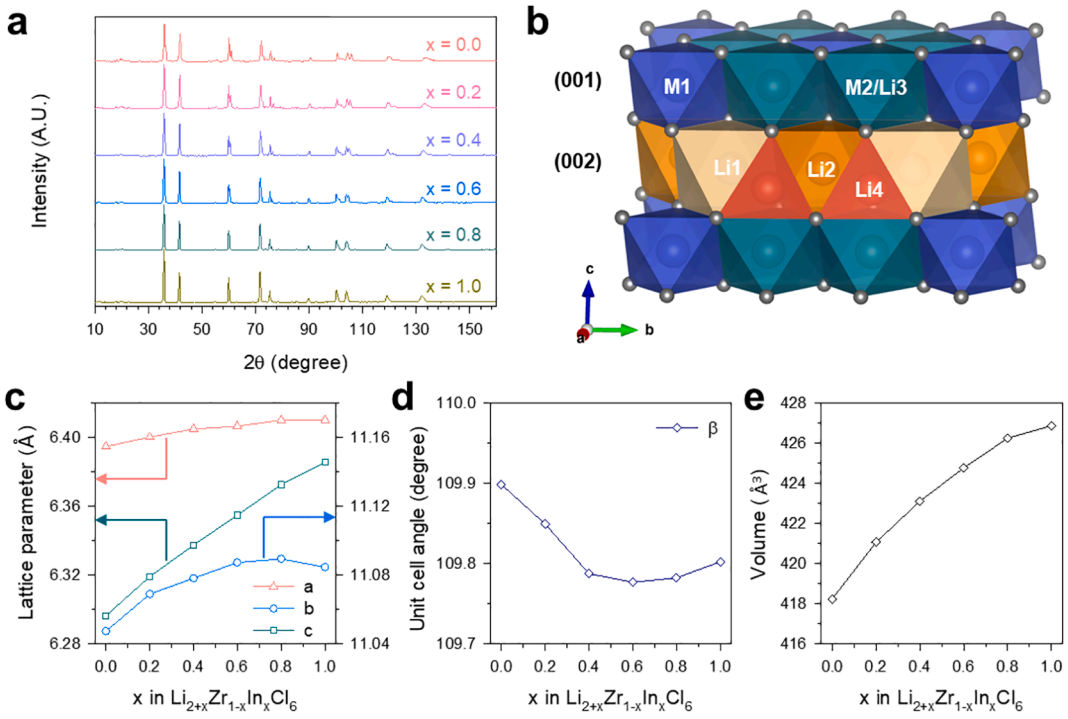

Fig. 1. Characterization of $Li_{2+x}Zr_{1-x}In_xCl_6$. a) Powder ND patterns and b) crystal structure of $Li_{2+x}Zr_{1-x}In_xCl_6$ ($0.0 \leq x \leq 1.0$). c) Lattice parameters, d) unit cell angle, and e) lattice volume of $Li_{2+x}Zr_{1-x}In_xCl_6$ as a function of the amount of doped In (x).

[30]. In this regard, the increased covalency of the Zr/M−Cl bond in $Li_{2+x}Zr_{1-x}M_xCl_6$ upon substitution is expected to be responsible for the distortion of the crystal structure. The anisotropic changes of the M−Cl bond lengths in the M1 octahedra are shown in Figure S4.

To investigate Li^+ migration in In^{3+}-substituted Li_2ZrCl_6 from a structural point of view, Rietveld refinements of the powder ND data were carried out. Five distinct polyhedra are shown in Fig. 2a. Powder ND Rietveld refinement profiles for $Li_{2+x}Zr_{1-x}M_xCl_6$ are shown in Figure S5, and the refinement results are summarized in Table S1–S6. The polyhedral volume and occupancies of M and Li are shown in Fig. 2b

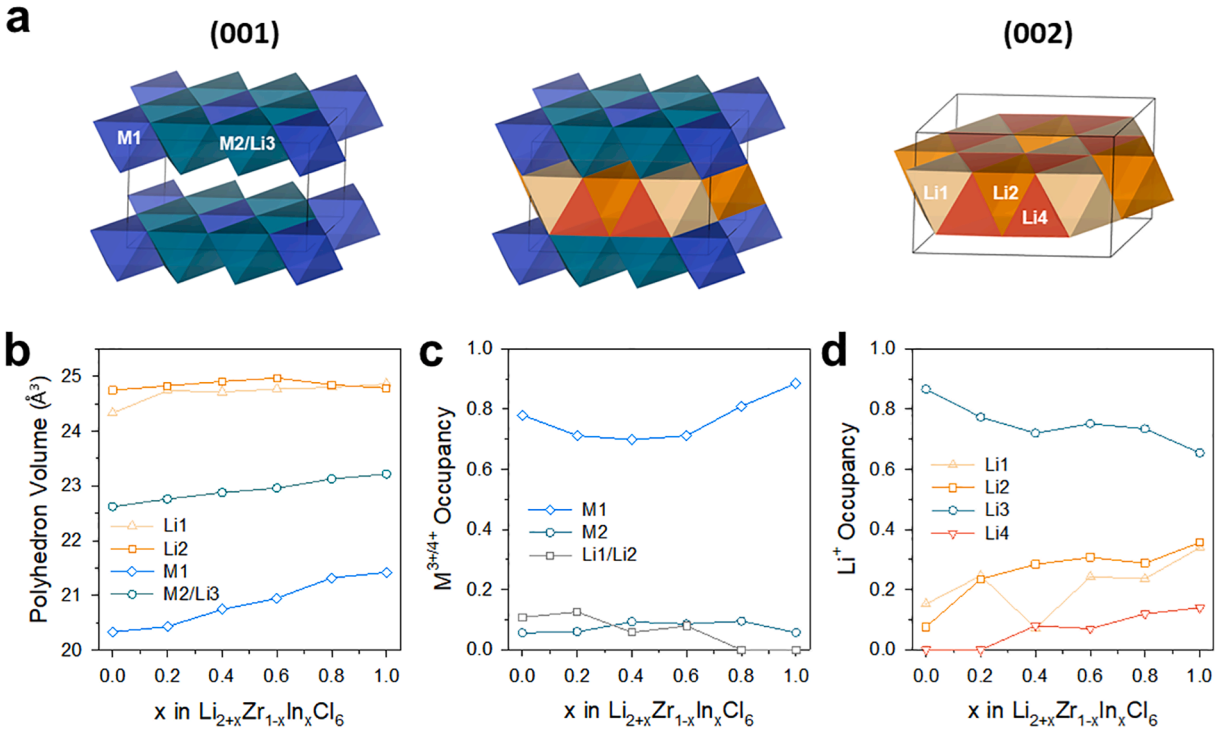

Fig. 2. Structural characterization of polyhedra in $Li_{2+x}Zr_{1-x}In_xCl_6$. a) Crystal structure of $Li_{2+x}Zr_{1-x}In_xCl_6$ with the unit cell outlined. In (001) plane (left), isolated [Zr/In]Cl_6 octahedra are located in the ab-plane at z = 0 and surrounded by six Li^+ ions that form a honeycomb lattice of $LiCl_6$ octahedra, where the metal is partially occupied. Two kinds of $LiCl_6$ octahedra and one kind of $LiCl_4$ tetrahedra are located in the ab-plane at z = 0.5 (right). b) Polyhedron volume and occupancies of c) central metal and d) Li, as a function of the amount of doped In (x).

and c, respectively. In unsubstituted Li_2ZrCl_6, the Zr^{4+} mainly occupies the M1 site (~0.78, Wyckoff position 2a) and partially occupies the M2 site (~0.05, Wyckoff position 4g). Additionally, Zr^{4+} was also present at Li1 and Li2 sites (~0.1, Wyckoff positions at 2d and 4h, respectively) belonging to the (002) plane, which is distinctly different from the monoclinic Li_3InCl_6. For the series of $Li_{2+x}Zr_{1-x}M_xCl_6$ up to $x = 0.6$, decreased occupancy of Zr^{4+} and increased occupancy of In^{3+} in the M1 site was observed (Figure S6). However, at $x > 0.6$, In^{3+} occupied M2 sites as well, and the Zr^{4+} in the M2 sites disappeared.

In Li_2ZrCl_6, despite the repulsive forces by metal cations at the M1 site, Li^+ ions are mainly present at the neighboring M2/Li3 site in the (001) plane (Fig. 2d). In contrast, Li^+ was rarely present in the Li1, Li2, and Li4 sites in the (002) plane. Although the aliovalent substitution of Li_2ZrCl_6 with In^{3+} leads to an overall increase in Li^+ concentration in the lattice, the occupancy of Li3 site in the (001) plane decreased upon substitution. Instead, occupancies for Li1 and Li2 sites belonging to the (002) plane was increased. Further, starting at $x \geq 0.4$, the tetrahedral Li site (Li4), which shares faces with all octahedral Li sites, was occupied. Overall, the In-substitution rendered the redistribution of Li^+ specifically to increase the Li^+ concentration in the (002) plane. This rearrangement is considered to facilitate Li^+ migration in the *ab*-plane, and is discussed later.

To obtain an in-depth understanding of the Li^+ migration in $Li_{2+x}Zr_{1-x}M_xCl_6$, BVEL calculations were also carried out (Fig. 3). BVEL calculations have been effectively used to probe ion migration pathways [24,25,30,46,47]. The BVEL map and energy landscape diagram of Li_2ZrCl_6 obtained using structural parameters from the ND Rietveld refinement results (Table S1) is shown in Fig. 3a and 3b. It visualizes the possible Li^+ migration pathways using the ball-and-stick illustration (Fig. 3c–f). Li^+ could migrate through 3D pathways, and all Li^+ migration pathways were formed through the octahedral Li sites bridged by interstitial tetrahedral Li4 sites. Since the interstitial Li4 sites share faces with all octahedral Li sites, 3D Li^+ migration is possible. These Li^+ migration pathways are composed of three unique pathways: Li1-Li4-Li2 (path 1), Li2-Li4-Li2 (path 2), and Li3-Li4-(Li1/Li2)-Li4-Li3 (path 3). In the *ab*-plane view at $z \approx 0.5$, three distinct Li sites create 2D migration pathways with low activation energies of 0.483 and 0.456 eV (Fig. 3c and 3d). The activation energy for the Li3-Li4-(Li1/Li2)-Li4-Li3 pathway along the *c*-axis was 0.509 eV (Fig. 3e and 3f). These results indicate a 2D-preferable 3D Li migration feature, which is consistent with previously reported results [48]. Since the BVEL calculations consider only the crystal structure of immobile ions, understanding the Li^+ migration mechanism in aliovalent-substituted materials more accurately requires theoretical calculations [48].

Variation in Li^+ conductivity at 30 °C as a function of M^{3+} substitution (x) in a series of $Li_{2+x}Zr_{1-x}M_xCl_6$ is shown in Fig. 4. Li^+

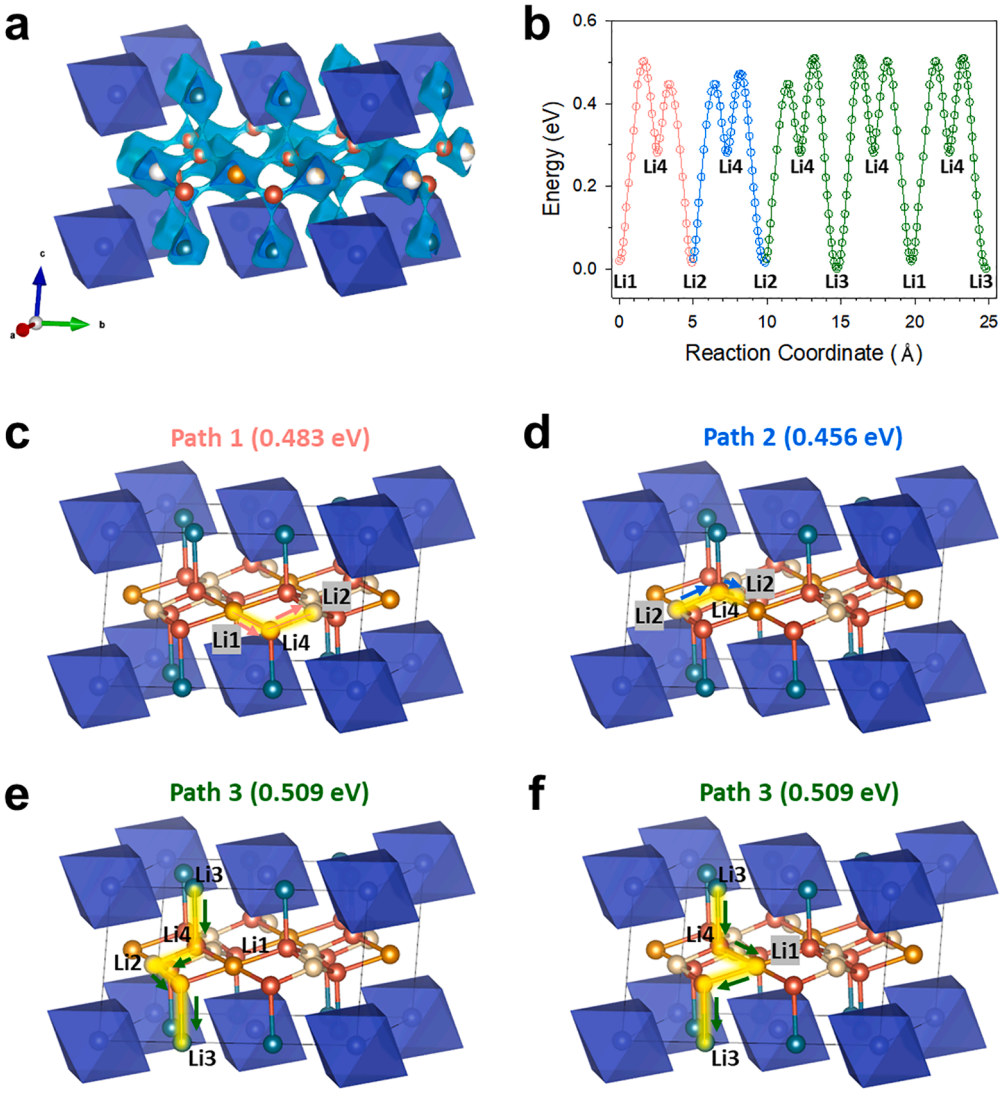

Fig. 3. BVEL calculation results of $Li_{2+x}Zr_{1-x}In_xCl_6$. a) Li^+ diffusion paths of $Li_{2+x}Zr_{1-x}In_xCl_6$ with an *iso*-surface value of ± 0.5 v.u. b) Energy landscape diagram of $Li_{2+x}Zr_{1-x}In_xCl_6$, showing migration barriers between Li^+ and interstitial sites. c–f) Possible Li^+ conduction paths.

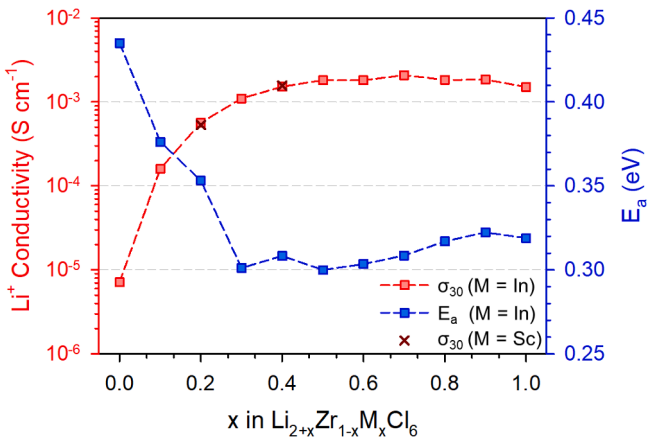

Fig. 4. Li^+ conductivities at 30 °C and activation energies for M^{3+}-substituted Li_2ZrCl_6 as a function of x in $Li_{2+x}Zr_{1-x}M^{3+}{}_xCl_6$ (M = In, Sc).

conductivities were obtained by fitting Nyquist plots of Li^+-blocking Ti/$Li_{2+x}Zr_{1-x}M_xCl_6$/Ti symmetric cells with cold-pressed SE pellets. The activation energies obtained from the Arrhenius plots are also shown in Figure S7. The Li^+ conductivity for unsubstituted monoclinic Li_2ZrCl_6 was 7.1×10^{-6} S cm^{-1} (activation energy of 0.435 eV), consistent with previously reported values and considerably lower than those of isostructural counterparts of Li_3InCl_6 (1.5 mS cm^{-1}) and Li_3ScCl_6 (3.0 mS cm^{-1}) [26,29,38]. Although the smaller charge carrier concentration of Li^+ in Li_2ZrCl_6 than those in Li_3InCl_6 and Li_3ScCl_6 is considered a main factor contributing to the large difference in Li^+ conductivity, the effects of lattice volume (418.24 (3) $Å^3$ (Li_2ZrCl_6) vs. 426.409 $Å^3$ (Li_3InCl_6) and 420.730 $Å^3$ (Li_3ScCl_6)) cannot be neglected. As the amount of M^{3+} substituted in $Li_{2+x}Zr_{1-x}M_xCl_6$ increased, Li^+ conductivity drastically increased by more than three orders of magnitude, up to $x = 0.4$ and reached a maximum value of 2.1 mS cm^{-1} at $x = 0.7$ with a corresponding activation energy of 0.309 eV. Upon subsequent substitution of $x > 0.7$, the Li^+ conductivity was almost saturated. The positive effects of aliovalent substitution and optimal Li concentration in halide superionic conductors were also observed in $Li_{3-x}Y_{1-x}Zr_xCl_6$, $Li_{3-x}Yb_{1-x}Hf_xCl_6$, $Li_{2+x}Zr_{1-x}Fe_xCl_6$, and $Na_{3-x}(Y/Er)_{1-x}Zr_xCl_6$ [27,29,36,49,50].

The drastic increase in Li^+ conductivity of Li_2ZrCl_6 by aliovalent substitution can be explained by considering several factors. First, the insufficient amount of mobile charge carriers of Li^+ in Li_2ZrCl_6, compared to those in Li_3InCl_6 and Li_3ScCl_6, specifically explains the low Li^+ concentration in the *ab*-plane at $z \approx 0.5$, as analyzed from the ND Rietveld refinement results (Fig. 2). Importantly, for Li_2ZrCl_6, Li^+ is absent in the interstitial Li4 site, which is the core of the 3D Li^+ migration pathways. This feature is a significant disadvantage not only for the intra-layer Li^+ migration in the *ab*-plane at $z \approx 0.5$, but also for the interlayer Li^+ migration along the *c*-axis (Fig. 3). Second, the redistribution of Li^+ in the lattice driven by aliovalent substitution could also render the energy landscape for Li^+ migration as more favorable [25,39]. Third, the increased covalent character of M−Cl bonds that induce anisotropic lattice expansion may play a beneficial role in Li^+ migration. According to a recent theoretical study, using first-principles molecular dynamics coupled with Wannier analysis, the Li_3InBr_6 and similar halide SEs which have mixed ionic–covalent bonding characteristics could provide facile Li^+ migration by modulating the overall potential energy landscape [51]. In this regard, the well-balanced and mixed ionic–covalent bonding characteristics of Zr–Cl and In(or Sc)–Cl bonds in $Li_{2+x}Zr_{1-x}M_xCl_6$ may be responsible for the enhanced ionic conductivity [30].

The electrochemical stability of $Li_{2.5}Zr_{0.5}In_{0.5}Cl_6$ was assessed by cyclic voltammetry (CV) measurements using Ti/($Li_{2.5}Zr_{0.5}In_{0.5}Cl_6$/Super C65)/$Li_{2.5}Zr_{0.5}In_{0.5}Cl_6$/$Li_6PS_5Cl$/Li-In cells (Figure S8). $Li_{2.5}Zr_{0.5}In_{0.5}Cl_6$ showed poor cathodic stability with the onset voltage of ~ 2.1 V (vs. Li/Li^+) but excellent oxidation stability up to 5 V (vs. Li/Li^+), which is in line with previous results of other halide SEs [27,33,35,38,52,53].

Finally, the applicability of $Li_{2.5}Zr_{0.5}In_{0.5}Cl_6$ (1.8 mS cm^{-1}), compared to the mechanochemically prepared Li_2ZrCl_6 (referred to as "BM-Li_2ZrCl_6", 0.4 mS cm^{-1}) for uncoated single-NCM88 was assessed in all-solid-state cells at 30 °C (Fig. 5). Fig. 5a shows the first charge–discharge voltage profiles at 0.1C. Single-NCM88 electrodes employing BM-Li_2ZrCl_6 and $Li_{2.5}Zr_{0.5}In_{0.5}Cl_6$ showed the high first discharge capacities of 207 and 202 mA h g^{-1} with the high initial Columbic efficiencies of 87.1% and 87.2%, respectively. These results are indebted to the synergetic effects of oxidation-tolerable halide SE and cracking-free single-crystal cathode active material [29,36,54,55]. At higher C-rates (Fig. 5b), the electrodes using $Li_{2.5}Zr_{0.5}In_{0.5}Cl_6$ outperformed those using BM-Li_2ZrCl_6, which is attributed to the higher Li^+ conductivity of $Li_{2.5}Zr_{0.5}In_{0.5}Cl_6$ than that of BM-Li_2ZrCl_6. Further, single-NCM88/Li-In all-solid-state cells using $Li_{2.5}Zr_{0.5}In_{0.5}Cl_6$ showed an acceptable capacity retention of 86.4% after 100 cycles (3rd/102nd cycle, inset in Fig. 5b). The excellent performance of the single-NCM88 electrodes is attributed to the synergetic effect of cracking-free features of the single-crystalline cathode materials and oxidation tolerance of $Li_{2.5}Zr_{0.5}In_{0.5}Cl_6$ [36].

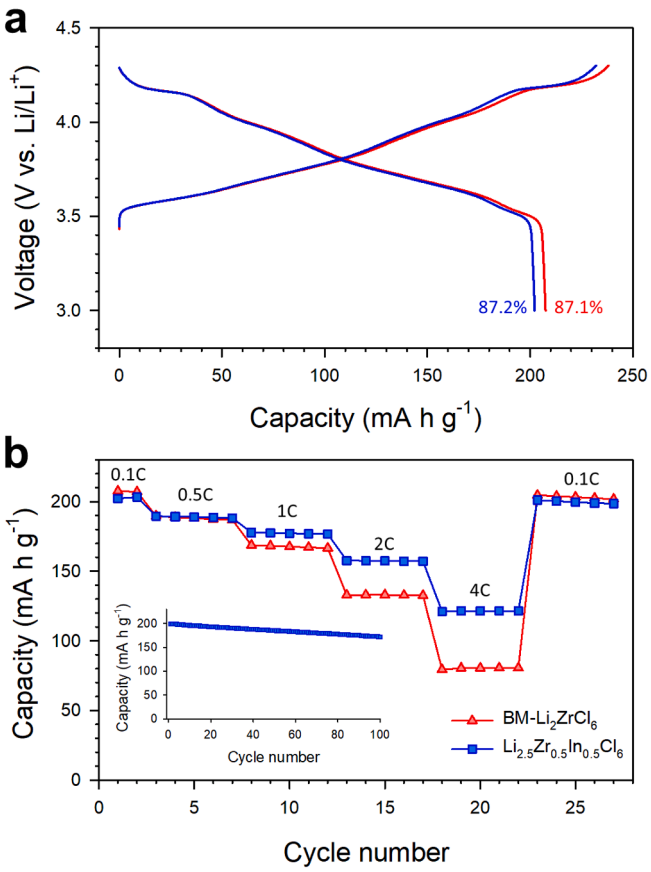

Fig. 5. Electrochemical performance results at 30 °C for single-NCM88/Li-In all-solid-state cells using BM-Li_2ZrCl_6 and $Li_{2.5}Zr_{0.5}In_{0.5}Cl_6$ at 30 °C. a) First charge–discharge voltage profile at 0.1C (1C = 200 mA g^{-1}) for single-NCM88 electrodes using $Li_{2.5}Zr_{0.5}In_{0.5}Cl_6$ or BM-Li_2ZrCl_6. b) Rate capabilities of the single-NCM88 electrodes using $Li_{2.5}Zr_{0.5}In_{0.5}Cl_6$ or BM-Li_2ZrCl_6. Cycling performance of the single-NCM88 electrodes using $Li_{2.5}Zr_{0.5}In_{0.5}Cl_6$ at 0.5C at a constant current–constant voltage mode (a limiting current of 0.05C) is also shown in the inset of (b).

3. Conclusions

In summary, Li^+-conducting halide SEs of $Li_{2+x}Zr_{1-x}M_xCl_6$ (M = In, Sc) with a maximum Li^+ conductivity of 2.1 mS cm^{-1} ($x = 0.70$) was investigated. The solid solution monoclinic structure with *C*2/*m* symmetry was confirmed over the entire range of *x*. Structural analysis by Rietveld ND and XRD refinements revealed the dynamic redistribution of Li^+ in the lattice upon aliovalent substitution. In other words, the significantly increased occupancy in the Li sites in the (0 0 2) plane and occurrence of Li^+ in the tetrahedral interstitial site explain the increase in Li^+ conductivity by more than two orders of magnitude. Moreover, the aliovalent substitution induced lattice distortion, which could be attributed to the effects of the ionic or covalent characteristics of the M−Cl bonds. The BVEL calculations revealed the 2D-preferable 3D Li^+ migration pathways via tetrahedrally coordinated Li^+ interstitial sites. Finally, the excellent feasibility of $Li_{2+x}Zr_{1-x}In_xCl_6$ as a catholyte for single-NCM88 electrodes in all-solid-state cells was successfully demonstrated. Our results provide an important insight for the design of new halide superionic conductors in terms of Li^+ migration in lattices.

4. Experimental

4.1. Preparation of materials

To prepare $Li_{2+x}Zr_{1-x}M_xCl_6$, a stoichiometric mixture of LiCl (99.99%, Sigma Aldrich), $ZrCl_4$ (99.99%, Sigma Aldrich), $ScCl_3$ (99.9%, Alfa Aesasr), and $InCl_3$ (99.99%, Alfa Aesasr) was ball-milled at 600 rpm for 10 h in a ZrO_2 vial with ZrO_2 balls using Pulverisette 7PL (Fritsch GmbH). The ball-milled powders were then heated to 260 °C for 12 h in a fused silica ampoule sealed under vacuum. To prepare Li_6PS_5Cl, a stoichiometric mixture of Li_2S (99.9%, Alfa Aesar), P_2S_5 (99%, Sigma Aldrich), and LiCl (99.99%, Sigma Aldrich) was ball-milled at 600 rpm for 10 h in a ZrO_2 vial with ZrO_2 balls, followed by heating at 550 °C for 5 h under an Ar atmosphere.

4.2. Materials characterization

Powder XRD patterns were obtained using a Rigaku MiniFlex600 diffractometer with Cu K_α radiation ($\lambda = 1.5406$ Å). XRD cells containing hermetically sealed SE samples with a beryllium window were mounted on an XRD diffractometer and measured at 40 kV and 15 mA. The neutron powder diffraction data were obtained from the HANARO facility at the Korea Atomic Energy Research Institute (KAERI). The measurements were conducted in the 2θ range of 0–160° with a step size of 0.05° using a wavelength of 1.834707 Å. High-resolution powder X-ray diffraction (HRPD) data were acquired at the 9B beamline in the Pohang Accelerator Laboratory (PAL, South Korea) using monochromatic X-rays ($\lambda = 1.5220$ Å). X-ray and neutron diffraction data were refined by the Rietveld refinement method using Fullprof software.

4.3. Electrochemical characterization

Li^+ conductivities were measured by AC impedance method using Li^+-blocking Ti/SE/Ti symmetric cells. The cold-pressed pellets were prepared at a pressure of 370 MPa. The EIS data were recorded at an amplitude of 10 mV and a frequency range from 10 mHz to 7 MHz using a VMP3 (Bio-Logic). For the fabrication of all-solid-state half-cells, Li-In electrodes were used as both the counter and reference electrodes. After preparing Li-In powders by ball-milling In (Aldrich, 99%) and Li (FMC Lithium Corp.) with a nominal composition of $Li_{0.5}In$, they were mixed with Li_6PS_5Cl powders in a weight ratio of 8:2. Further, 150 mg of Li_6PS_5Cl powders were pelletized under 100 MPa to form SE layers. Composite working electrodes were prepared from a mixture of single-NCM88, $Li_{2.5}Zr_{0.5}In_{0.5}Cl_6$, and super C65 at a weigh ratio of 70:50:3, respectively. The mass loading of single-NCM88 was 6.4 mg cm^{-2}, which translates into the areal capacity of ~ 1.3 mA h cm^{-2}. Finally, the single-NCM88 electrodes and Li-In electrodes were attached to both sides of the SE layers, and the entire assembly was pressed at 370 MPa. The all-solid-state cells were tested under an external pressure of ~ 70 MPa. The CV measurements were carried out using Ti/($Li_{2.5}Zr_{0.5}In_{0.5}Cl_6$/Super C65)/$Li_{2.5}Zr_{0.5}In_{0.5}Cl_6$/$Li_6PS_5Cl$/Li-In cells under ~ 70 MPa.

Declaration of Competing Interest

The authors declare that they have no known competing financial interests or personal relationships that could have appeared to influence the work reported in this paper.

Acknowledgements

This research was supported by the Technology Development Program to Solve Climate Changes and by Basic Science Research Program of the National Research Foundation (NRF) funded by the Ministry of Science & ICT (grant no. 2018R1A2B6004996 and 2017M1A2A2044501), and by the Materials and Components Technology Development Program of MOTIE/KEIT (grant no. 10077709 and 20007045). The work was also funded by the Yonsei University Research Fund of 2021 (2021-22-0326).

Appendix A. Supplementary data

Supplementary data to this article can be found online at https://doi.org/10.1016/j.cej.2022.135413.

References

[1] A.M. Abakumov, S.S. Fedotov, E.V. Antipov, J.M. Tarascon, Solid state chemistry for developing better metal-ion batteries, Nat. Commun. 11 (2020) 4976, https://doi.org/10.1038/s41467-020-18736-7.
[2] J. Janek, W.G. Zeier, A solid future for battery development, Nat. Energy 1 (2016) 16141, https://doi.org/10.1038/nenergy.2016.141.
[3] Y. Kato, S. Hori, T. Saito, K. Suzuki, M. Hirayama, A. Mitsui, M. Yonemura, H. Iba, R. Kanno, High-power all-solid-state batteries using sulfide superionic conductors, Nat. Energy 1 (2016) 16030, https://doi.org/10.1038/nenergy.2016.30.
[4] X. Han, Y. Gong, K.(. Fu, X. He, G.T. Hitz, J. Dai, A. Pearse, B. Liu, H. Wang, G. Rubloff, Y. Mo, V. Thangadurai, E.D. Wachsman, L. Hu, Negating interfacial impedance in garnet-based solid-state Li metal batteries, Nat. Mater. 16 (5) (2017) 572–579, https://doi.org/10.1038/nmat4821.
[5] K. Kerman, A. Luntz, V. Viswanathan, Y.-M. Chiang, Z. Chen, Review—Practical Challenges Hindering the Development of Solid State Li Ion Batteries, J. Electrochem. Soc. 164 (7) (2017) A1731–A1744, https://doi.org/10.1149/2.1571707jes.
[6] A. Manthiram, X. Yu, S. Wang, Lithium battery chemistries enabled by solid-state electrolytes, Nat. Rev. Mater. 2 (2017) 16103, https://doi.org/10.1038/natrevmats.2016.103.
[7] K.H. Park, Q. Bai, D.H. Kim, D.Y. Oh, Y. Zhu, Y. Mo, Y.S. Jung, Design Strategies, Practical Considerations, and New Solution Processes of Sulfide Solid Electrolytes for All-Solid-State Batteries, Adv. Energy Mater. 8 (18) (2018) 1800035, https://doi.org/10.1002/aenm.201800035.
[8] Z. Zhang, Y. Shao, B. Lotsch, Y.-S. Hu, H. Li, J. Janek, L.F. Nazar, C.-W. Nan, J. Maier, M. Armand, L. Chen, New horizons for inorganic solid state ion conductors, Energy Environ. Sci. 11 (8) (2018) 1945–1976, https://doi.org/10.1039/C8EE01053F.
[9] F. Han, A.S. Westover, J. Yue, X. Fan, F. Wang, M. Chi, D.N. Leonard, N.J. Dudney, H. Wang, C. Wang, High electronic conductivity as the origin of lithium dendrite formation within solid electrolytes, Nat. Energy 4 (3) (2019) 187–196, https://doi.org/10.1038/s41560-018-0312-z.
[10] R. Chen, Q. Li, X. Yu, L. Chen, H. Li, Approaching Practically Accessible Solid-State Batteries: Stability Issues Related to Solid Electrolytes and Interfaces, Chem. Rev. 120 (14) (2020) 6820–6877, https://doi.org/10.1021/acs.chemrev.9b00268.
[11] D. Cao, X. Sun, Q. Li, A. Natan, P. Xiang, H. Zhu, Lithium Dendrite in All-Solid-State Batteries: Growth Mechanisms, Suppression Strategies, and Characterizations, Matter 3 (1) (2020) 57–94, https://doi.org/10.1016/j.matt.2020.03.015.
[12] H.-J. Deiseroth, S.-T. Kong, H. Eckert, J. Vannahme, C. Reiner, T. Zaiß, M. Schlosser, Li_6PS_5X: a class of crystalline Li-rich solids with an unusually high Li^+ mobility, Angew. Chem. Int. Ed. 120 (4) (2008) 767–770, https://doi.org/10.1002/ange.200703900.
[13] S. Stramare, V. Thangadurai, W. Weppner, Lithium Lanthanum Titanates: A Review, Chem. Mater. 15 (2003) 3974–3990, https://doi.org/10.1021/cm0300516.

[14] S. Kim, H. Oguchi, N. Toyama, T. Sato, S. Takagi, T. Otomo, D. Arunkumar, N. Kuwata, J. Kawamura, S.I. Orimo, A complex hydride lithium superionic conductor for high-energy-density all-solid-state lithium metal batteries, Nat. Commun. 10 (2019) 1081, https://doi.org/10.1038/s41467-019-09061-9.

[15] L. Duchêne, A. Remhof, H. Hagemann, C. Battaglia, Status and prospects of hydroborate electrolytes for all-solid-state batteries, Energy Storage Mater. 25 (2020) 782–794, https://doi.org/10.1016/j.ensm.2019.08.032.

[16] T. Asano, A. Sakai, S. Ouchi, M. Sakaida, A. Miyazaki, S. Hasegawa, Solid Halide Electrolytes with High Lithium-Ion Conductivity for Application in 4 V Class Bulk-Type All-Solid-State Batteries, Adv. Mater. 30 (44) (2018) 1803075, https://doi.org/10.1002/adma.201803075.

[17] K.H. Kim, Y. Iriyama, K. Yamamoto, S. Kumazaki, T. Asaka, K. Tanabe, C.A. J. Fisher, T. Hirayama, R. Murugan, Z. Ogumi, Characterization of the interface between $LiCoO_2$ and $Li_7La_3Zr_2O_{12}$ in an all-solid-state rechargeable lithium battery, J. Power Sources 196 (2) (2011) 764–767, https://doi.org/10.1016/j.jpowsour.2010.07.073.

[18] Y. Zhu, X. He, Y. Mo, Origin of Outstanding Stability in the Lithium Solid Electrolyte Materials: Insights from Thermodynamic Analyses Based on First-Principles Calculations, ACS Appl. Mater. Interfaces 7 (42) (2015) 23685–23693, https://doi.org/10.1021/acsami.5b07517.

[19] J. van den Broek, S. Afyon, J.L.M. Rupp, Interface-Engineered All-Solid-State Li-Ion Batteries Based on Garnet-Type Fast Li^+ Conductors, Adv. Energy Mater. 6 (19) (2016) 1600736, https://doi.org/10.1002/aenm.201600736.

[20] A. Sakuda, A. Hayashi, M. Tatsumisago, Interfacial Observation between $LiCoO_2$ Electrode and Li_2S−P_2S_5 Solid Electrolytes of All-Solid-State Lithium Secondary Batteries Using Transmission Electron Microscopy†, Chem. Mater. 22 (3) (2010) 949–956, https://doi.org/10.1021/cm901819c.

[21] S.H. Jung, K. Oh, Y.J. Nam, D.Y. Oh, P. Brüner, K. Kang, Y.S. Jung, Li_3BO_3–Li_2CO_3: Rationally Designed Buffering Phase for Sulfide All-Solid-State Li-Ion Batteries, Chem. Mater. 30 (22) (2018) 8190–8200, https://doi.org/10.1021/acs.chemmater.8b0332110.1021/acs.chemmater.8b03321.s001.

[22] X. Chen, Z. Guan, F. Chu, Z. Xue, F. Wu, Y. Yu, Air-stable inorganic solid-state electrolytes for high energy density lithium batteries: Challenges, strategies, and prospects, InfoMat (2021) 1–20, https://doi.org/10.1002/inf2.12248.

[23] K.H. Park, D.Y. Oh, Y.E. Choi, Y.J. Nam, L. Han, J.-Y. Kim, H. Xin, F. Lin, S.M. Oh, Y.S. Jung, Solution-Processable Glass LiI-Li_4SnS_4 Superionic Conductors for All-Solid-State Li-Ion Batteries, Adv. Mater. 28 (9) (2016) 1874–1883, https://doi.org/10.1002/adma.201505008.

[24] A. Banerjee, K.H. Park, J.W. Heo, Y.J. Nam, C.K. Moon, S.M. Oh, S.-T. Hong, Y. S. Jung, Na3SbS4: A Solution Processable Sodium Superionic Conductor for All-Solid-State Sodium-Ion Batteries, Angew. Chem. Int. Ed. 128 (33) (2016) 9786–9790, https://doi.org/10.1002/ange.201604158.

[25] H. Kwak, K.H. Park, D. Han, K.-W. Nam, H. Kim, Y.S. Jung, Li^+ conduction in air-stable Sb-Substituted Li_4SnS_4 for all-solid-state Li-Ion batteries, J. Power Sources 446 (2020) 227338, https://doi.org/10.1016/j.jpowsour.2019.227338.

[26] X. Li, J. Liang, J. Luo, M. Norouzi Banis, C. Wang, W. Li, S. Deng, C. Yu, F. Zhao, Y. Hu, T.-K. Sham, L.i. Zhang, S. Zhao, S. Lu, H. Huang, R. Li, K.R. Adair, X. Sun, Air-stable Li_3InCl_6 electrolyte with high voltage compatibility for all-solid-state batteries, Energy Environ. Sci. 12 (9) (2019) 2665–2671, https://doi.org/10.1039/C9EE02311A.

[27] K.-H. Park, K. Kaup, A. Assoud, Q. Zhang, X. Wu, L.F. Nazar, High-Voltage Superionic Halide Solid Electrolytes for All-Solid-State Li-Ion Batteries, ACS Energy Lett. 5 (2) (2020) 533–539, https://doi.org/10.1021/acsenergylett.9b0259910.1021/acsenergylett.9b02599.s001.

[28] L. Zhou, C.Y. Kwok, A. Shyamsunder, Q. Zhang, X. Wu, L.F. Nazar, A new halospinel superionic conductor for high-voltage all solid state lithium batteries, Energy Environ. Sci. 13 (7) (2020) 2056–2063, https://doi.org/10.1039/D0EE01017K.

[29] H. Kwak, D. Han, J. Lyoo, J. Park, S.H. Jung, Y. Han, G. Kwon, H. Kim, S.-T. Hong, K.-W. Nam, Y.S. Jung, New Cost-Effective Halide Solid Electrolytes for All-Solid-State Batteries: Mechanochemically Prepared Fe^{3+}-Substituted Li_2ZrCl_6, Adv. Energy Mater. 11 (12) (2021) 2003190, https://doi.org/10.1002/aenm.202003190.

[30] H. Kwak, J. Lyoo, J. Park, Y. Han, R. Asakura, A. Remhof, C. Battaglia, H. Kim, S.-T. Hong, Y.S. Jung, Na_2ZrCl_6 enabling highly stable 3 V all-solid-state Na-ion batteries, Energy Storage Mater. 37 (2021) 47–54, https://doi.org/10.1016/j.ensm.2021.01.026.

[31] Z. Liu, S. Ma, J. Liu, S. Xiong, Y. Ma, H. Chen, High Ionic Conductivity Achieved in $Li_3Y(Br\ 3C_l3)$ Mixed Halide Solid Electrolyte via Promoted Diffusion Pathways and Enhanced Grain Boundary, ACS Energy Lett. 6 (1) (2021) 298–304, https://doi.org/10.1021/acsenergylett.0c0169010.1021/acsenergylett.0c01690.s001.

[32] H. Ito, K. Shitara, Y. Wang, K. Fujii, M. Yashima, Y. Goto, C. Moriyoshi, N. C. Rosero-Navarro, A. Miura, K. Tadanaga, Kinetically Stabilized Cation Arrangement in Li_3YCl_6 Superionic Conductor during Solid-State Reaction, Adv. Sci. 8 (15) (2021) 2101413, https://doi.org/10.1002/advs.202101413.

[33] S. Wang, Q. Bai, A.M. Nolan, Y. Liu, S. Gong, Q. Sun, Y. Mo, Lithium Chlorides and Bromides as Promising Solid-State Chemistries for Fast Ion Conductors with Good Electrochemical Stability, Angew. Chem. Int. Ed. 58 (24) (2019) 8039–8043, https://doi.org/10.1002/anie.201901938.

[34] A. Bohnsack, F. Stenzel, A. Zajonc, G. Balzer, M. S. Wickleder and G. Meyer, Ternäre Halogenide vom Typ A_3MX_6. VI [1]. Ternäre Chloride der Selten-Erd-Elemente mit Lithium, Li_3MCl_6 (M = Tb-Lu, Y, Sc): Synthese, Kristallstrukturen und Ionenbewegung, Z. anorg. allg. Chem., 623, (1997) 1067-1073. https://doi.org/10.1002/zaac.19976230710.

[35] X. Li, J. Liang, X. Yang, K.R. Adair, C. Wang, F. Zhao, X. Sun, Progress and Perspectives for Halide Solid-State Electrolyte for All-Solid-State Lithium Batteries, Energy Environ. Sci. 13 (2020) 1429–1461, https://doi.org/10.1039/C9EE03828K.

[36] J. Park, D. Han, H. Kwak, Y. Han, Y.J. Choi, K.-W. Nam, Y.S. Jung, Heat treatment protocol for modulating ionic conductivity via structural evolution of $Li_{3-x}Yb_{1-x}M_xCl_6$ (M = Hf^{4+}, Zr^{4+}) new halide superionic conductors for all-solid-state batteries, Chem. Eng. J. 425 (2021) 130630, https://doi.org/10.1016/j.cej.2021.130630.

[37] R. Schlem, S. Muy, N. Prinz, A. Banik, Y. Shao-Horn, M. Zobel, W.G. Zeier, Mechanochemical Synthesis: A Tool to Tune Cation Site Disorder and Ionic Transport Properties of Li_3MCl_6 (M = Y, Er) Superionic Conductors, Adv. Energy Mater. 10 (6) (2020) 1903719, https://doi.org/10.1002/aenm.201903719.

[38] J. Liang, X. Li, S. Wang, K.R. Adair, W. Li, Y. Zhao, C. Wang, Y. Hu, L.i. Zhang, S. Zhao, S. Lu, H. Huang, R. Li, Y. Mo, X. Sun, Site-Occupation-Tuned Superionic Li_xScCl_{3+x} Halide Solid Electrolytes for All-Solid-State Batteries, J. Am. Chem. Soc. 142 (15) (2020) 7012–7022, https://doi.org/10.1021/jacs.0c0013410.1021/jacs.0c00134.s001.

[39] B. Helm, R. Schlem, B. Wankmiller, A. Banik, A. Gautam, J. Ruhl, C. Li, M. R. Hansen, W.G. Zeier, Exploring Aliovalent Substitutions in the Lithium Halide Superionic Conductor $Li_{3-x}In_{1-x}Zr_xCl_6$ ($0 \le x \le 0.5$), Chem. Mater. 33 (12) (2021) 4773–4782, https://doi.org/10.1021/acs.chemmater.1c0134810.1021/acs.chemmater.1c01348.s00110.1021/acs.chemmater.1c01348.s002.

[40] J. Bréger, M. Jiang, N. Dupré, Y.S. Meng, Y. Shao-Horn, G. Ceder, C.P. Grey, High-resolution X-ray diffraction, DIFFaX, NMR and first principles study of disorder in the Li_2MnO_3–$Li[Ni_{1/2}Mn_{1/2}]O_2$ solid solution, J. Solid State Chem. 178 (9) (2005) 2575–2585, https://doi.org/10.1016/j.jssc.2005.05.027.

[41] J. Serrano-Sevillano, M. Reynaud, A. Saracibar, T. Altantzis, S. Bals, G. van Tendeloo, M. Casas-Cabanas, Enhanced electrochemical performance of Li-rich cathode materials through microstructural control, Phys. Chem. Chem. Phys. 20 (35) (2018) 23112–23122.

[42] C.H. Lei, J.G. Wen, M. Sardela, J. Bareño, I. Petrov, S.-H. Kang, D.P. Abraham, Structural study of Li_2MnO_3 by electron microscopy, J. Mater. Sci. 44 (20) (2009) 5579–5587, https://doi.org/10.1007/s10853-009-3784-1.

[43] X. Li, J. Liang, K.R. Adair, J. Li, W. Li, F. Zhao, Y. Hu, T.-K. Sham, L.i. Zhang, S. Zhao, S. Lu, H. Huang, R. Li, N. Chen, X. Sun, Origin of Superionic $Li_3Y_{1-x}In_xCl_6$ Halide Solid Electrolytes with High Humidity Tolerance, Nano Lett. 20 (6) (2020) 4384–4392, https://doi.org/10.1021/acs.nanolett.0c0115610.1021/acs.nanolett.0c01156.s001.

[44] Y. Shimakawa, Y. Kubo, Y. Tauchi, T. Kamiyama, H. Asano, F. Izumi, Structural distortion and ferroelectric properties of $SrBi_2(Ta_{1-x}Nb_x)_2O_9$, Appl. Phys. Lett. 77 (17) (2000) 2749–2751, https://doi.org/10.1063/1.1319509.

[45] T. Baidya, P. Bera, O. Kröcher, O. Safonova, P.M. Abdala, B. Gerke, R. Pöttgen, K. R. Priolkar, T.K. Mandal, Understanding the anomalous behavior of Vegard's law in $Ce_{1-x}M_xO_2$ (M= Sn and Ti; $0< x\le 0.5$) solid solutions, Phys. Chem. Chem. Phys. 18 (2016) 13974–13983, https://doi.org/10.1039/C6CP01525E.

[46] J.W. Heo, A. Banerjee, K.H. Park, Y.S. Jung, S.-T. Hong, New Na-Ion Solid Electrolytes $Na_{4-x}Sn_{1-x}Sb_xS_4$ ($0.02\le x\le 0.33$) for All-Solid-State Na-Ion Batteries, Adv. Energy Mater. 8 (11) (2018) 1702716, https://doi.org/10.1002/aenm.201702716.

[47] M. Avdeev, M. Sale, S. Adams, R.P. Rao, Screening of the alkali-metal ion containing materials from the Inorganic Crystal Structure Database (ICSD) for high ionic conductivity pathways using the bond valence method, Solid State Ion. 225 (2012) 43–46, https://doi.org/10.1016/j.ssi.2012.02.014.

[48] D. Park, H. Park, Y. Lee, S.-O. Kim, H.-G. Jung, K.Y. Chung, J.H. Shim, S. Yu, Theoretical Design of Lithium Chloride Superionic Conductors for All-Solid-State High-Voltage Lithium-Ion Batteries, ACS Appl. Mater. Interfaces 12 (31) (2020) 34806–34814, https://doi.org/10.1021/acsami.0c0700310.1021/acsami.0c07003.s001.

[49] R. Schlem, A. Banik, M. Eckardt, M. Zobel, W.G. Zeier, $Na_{3-x}Er_{1-x}Zr_xCl_6$—A Halide-Based Fast Sodium-Ion Conductor with Vacancy-Driven Ionic Transport, ACS Appl. Energy Mater. 3 (10) (2020) 10164–10173, https://doi.org/10.1021/acsaem.0c0187010.1021/acsaem.0c01870.s001.

[50] E.A. Wu, S. Banerjee, H. Tang, P.M. Richardson, J.-M. Doux, J. Qi, Z. Zhu, A. Grenier, Y. Li, E. Zhao, G. Deysher, E. Sebti, H. Nguyen, R. Stephens, G. Verbist, K.W. Chapman, R.J. Clément, A. Banerjee, Y.S. Meng, S.P. Ong, A stable cathode-solid electrolyte composite for high-voltage, long-cycle-life solid-state sodium-ion batteries, Nat. Commun. 12 (2021) 1256, https://doi.org/10.1038/s41467-021-21488-7.

[51] N. Adelstein, B.C. Wood, Role of Dynamically Frustrated Bond Disorder in a Li^+ Superionic Solid Electrolyte, Chem. Mater. 28 (20) (2016) 7218–7231, https://doi.org/10.1021/acs.chemmater.6b0079010.1021/acs.chemmater.6b00790.s00110.1021/acs.chemmater.6b00790.s002.

[52] W. Ji, D. Zheng, X. Zhang, T. Ding, D. Qu, A kinetically stable anode interface for Li_3YCl_6-based all-solid-state lithium batteries, J. Mater. Chem. A 9 (26) (2021) 15012–15018, https://doi.org/10.1039/D1TA03042F.

[53] L.M. Riegger, R. Schlem, J. Sann, W.G. Zeier, J. Janek, Lithium-Metal Anode Instability of the Superionic Halide Solid Electrolytes and the Implications for Solid-State Batteries, Angew. Chem. Int. Ed. 60 (12) (2021) 6718–6723, https://doi.org/10.1002/anie.202015238.

[54] Y. Han, S.H. Jung, H. Kwak, S. Jun, H.H. Kwak, J.H. Lee, S.-T. Hong, Y.S. Jung, Single- or Poly-Crystalline Ni-Rich Layered Cathode, Sulfide or Halide Solid Electrolyte: Which Will be the Winners for All-Solid-State Batteries? Adv. Energy Mater. 11 (21) (2021) 2100126, https://doi.org/10.1002/aenm.202100126.

[55] Y.B. Song, H. Kwak, W. Cho, K.S. Kim, Y.S. Jung, K.-H. Park, Electrochemo-Mechanical Effects as a Critical Design Factor for All-Solid-State Batteries, Curr. Opin. Solid State Mater. Sci. 26 (1) (2022) 100977, https://doi.org/10.1016/j.cossms.2021.100977.